

## Active Site, Catalytic Cycle, and Iodination Reactions of Vanadium Iodoperoxidase: A Computational Study

Luis F. Pacios<sup>\*,†</sup> and Oscar Gálvez<sup>‡</sup>

*Departamento de Biotecnología, Unidad de Química y Bioquímica, E.TSI Montes, Universidad Politécnica de Madrid, 28040 Madrid, Spain, and Departamento de Física Molecular, Instituto de Estructura de la Materia, C.S.I.C., Serrano 121, 28006 Madrid, Spain*

Received January 21, 2010

**Abstract:** A combined computational study using molecular surfaces and Poisson–Boltzmann electrostatic potentials for proteins and quantum calculations on complexes representing the vanadate cofactor throughout the catalytic cycle is employed to study the activity of vanadium iodoperoxidase (VIPO) from alga *Laminaria digitata*. A model structure of VIPO is compared with available crystal structures of chloroperoxidases (VCIPOs) and bromoperoxidases (VBrPOs) focusing on properties of the active site that concern halogen specificity. It is found that VIPO displays distinctive features regarding electrostatic potentials at the site cavity and the local topography of the cavity entrance. Quantum calculations on cofactor stages throughout the catalytic cycle reveal that, while steps involving binding of hydrogen peroxide and halide oxidization agree with available data on VBrPO, final formation and subsequent release of hypohalous acid could follow a different pathway consisting of His476-assisted protonation of bonded hypoiodite and further displacement by a water molecule. *Ab initio* free energies of reaction computed to explore iodination of organic substrates predict strongly exoergonic reactions with HOI, whereas other possible iodination reagents give thermodynamically disfavored reactions.

### Introduction

Atmospheric iodine and its potential role in the catalytic destruction of ozone have attracted considerable attention in the two past decades.<sup>1–3</sup> It has been shown that condensable iodine oxide vapors can nucleate efficiently to form aerosols, which may contribute to form cloud condensation nuclei and hence have an impact on the climate.<sup>4</sup> The most abundant oxide, IO, is formed after photolysis of reactive iodine precursors and subsequent reaction of I atoms with atmospheric O<sub>3</sub>. Recent measurements have shown high levels of IO in coastal Antarctica,<sup>5</sup> which, together with the relevance of iodine for atmospheric chemistry, opens the question of the release mechanisms required to account for such large amounts of iodine. High concentrations of IO have

been explained by a mechanism for iodine release triggered by the biological processing of iodide (I<sup>−</sup>) and the production of hypoiodous acid (HOI) from algae.<sup>3</sup> It is generally assumed that iodine in the atmosphere has a natural origin since no anthropogenic sources are known.<sup>6</sup> While low levels are found in soils, continental waters, and terrestrial plants, oceans are a major source. The iodine biogeochemical cycle involves large exchanges in the marine boundary layer (MBL) in which iodine is transferred from oceans to the atmosphere.<sup>7</sup> This process occurs by direct emission of I<sub>2</sub> and volatile iodinated compounds from open ocean (via phytoplankton) and coastal areas where macroalgae are a major contributor through the production of volatile iodocarbons.<sup>8</sup>

Large uncertainties still remain in assessing global emissions of volatile iodine compounds at the MBL in the iodine biogeochemical cycle, yet it is generally assumed that both seaweeds and marine phytoplankton release iodocarbons.<sup>9</sup>

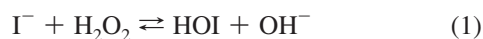
\* Corresponding author. E-mail: luis.fpacios@upm.es.

<sup>†</sup> Universidad Politécnica de Madrid.

<sup>‡</sup> C.S.I.C.

In coastal environments, brown macroalgae and especially kelps are considered as major contributors to the flux of iodine.<sup>10,11</sup> Kelp species such as *Laminaria digitata* are indeed the most effective iodine accumulators among all living systems.<sup>12</sup> In addition to iodinated organic compounds, IO is also detectable in the atmosphere above kelp beds,<sup>7b</sup> and it has been reported that kelps release I<sub>2</sub>, a major source of particle formation in coastal areas.<sup>13</sup> However, the reasons why seaweeds produce iodocarbons as well as the ecological significance of these compounds remain largely unknown. It has been recently shown that I<sup>−</sup> accumulation provides kelps with an inorganic antioxidant, the first described in living systems, that constitutes a protection against oxidative stress.<sup>11</sup>

In seawater, iodide reacts spontaneously with hydrogen peroxide to produce HOI:



but this reaction is slow. It was already observed in 1929 that this process occurs efficiently in cell walls of *L. digitata*, which led to the proposal of an “iodine oxidase” responsible for the catalyzed oxidation of iodide.<sup>14</sup> More recently, this oxidation has been confirmed to occur in the *Laminaria* apoplast where hypoiodous acid is formed virtually undissociated (pK = 10.64) at the pH of seawater, being itself in equilibrium with molecular iodine:<sup>12</sup>



Triiodide is in turn formed as the result of the equilibrium



but I<sub>2</sub>/I<sup>−</sup> complexation is weak in diluted solutions of iodide.<sup>10</sup> It is currently well established that the general catalytic role of halide oxidation in marine algae is actually played by vanadium-dependent haloperoxidases (VHPOs).<sup>10–13,15–18</sup> A VHPO enzyme specialized in oxidating iodide in cell walls of *L. digitata* should explain the high efficiency for iodine accumulation in this organism. Since both HOI and I<sub>2</sub> are more lipophilic than I<sup>−</sup>, their transport should be facilitated across membrane lipid bilayers at both iodine uptake and efflux occurring in response to biotic and abiotic stresses. Iodide detoxifies both aqueous (mainly hydrogen peroxide) and atmospheric (mainly ozone) oxidants,<sup>11</sup> and HOI is the central intermediate for all cases. In the absence of organic substrates, VHPOs catalyze the oxidation of a second equivalent of H<sub>2</sub>O<sub>2</sub>, resulting in the formation of singlet dioxygen and halide. In the presence of organic substrates, VHPOs catalyze the halogenation of a wide range of organic molecules.<sup>15</sup> The presence of these enzymes in the apoplast of marine algae could thus explain the production of I<sub>2</sub> and iodocarbons, compounds for which a defense function has been proposed on the basis of their high microbial toxicity.<sup>11,19</sup>

The majority of naturally occurring organohalogens and nearly all brominated and iodinated natural products are produced by marine organisms on a large scale.<sup>20</sup> Although the biogenesis of these compounds (many of them with

biological activities of pharmacological interest) has been studied for a long time, more new enzymes for halogenation have been discovered in the past five years than in the four decades before.<sup>18</sup> Haloperoxidases are major halogenating enzymes classified according to the most electronegative halide they oxidize. VHPOs, present in macroalgae, fungi, and bacteria, contain a ligated vanadate ion and use hydrogen peroxide to oxidize a halide (X<sup>−</sup>) to its corresponding hypohalous acid (HOX), an intermediate chemically equivalent to an electrophile reagent “X<sup>+</sup>”.<sup>17–19</sup> This reaction product has been customarily considered as a mixture of different species “X<sup>+</sup>” = HOX, X<sub>2</sub>, and X<sub>3</sub><sup>−</sup> all of them able to halogenate appropriate organic substrates if present.<sup>15–19</sup>

Crystal structures have been reported for H=Cl (VCIPO) haloperoxidase from the fungus *Curvularia inaequalis*,<sup>21,22</sup> H=Br (VBrPO) from the brown alga *Ascophyllum nodosum*,<sup>23</sup> and VBrPO from the red alga *Corallina officinalis*.<sup>24</sup> Kinetics and structural studies of peroxide-bound forms and mutants of VCIPO as well as mutants of VBrPO have been also developed.<sup>25</sup> All these studies have led to a general consensus regarding the role of the residues that bind the vanadate cofactor within the active site.<sup>17,18</sup> However, for H=I (VIPO) haloperoxidases, no experimental structure is available. A distinct vanadium-dependent iodoperoxidase has been purified from *L. digitata*, and kinetic studies have shown that it oxidizes iodide specifically, although competition experiments indicate that bromide is a competitive inhibitor.<sup>16</sup> This VIPO is the obvious candidate to explain not only iodine uptake and efflux observed in kelps but also the formation of iodocarbons released by these algae. The amino acid sequence of *L. digitata* VIPO shows the conserved residues in the active site of all VHPOs except two significant differences, one with respect to VCIPOs and another with respect to VBrPOs, which point to specific features that are discussed below.

Since the resolution of crystal structures of these proteins precludes solving hydrogen atoms from experimental electron densities, details regarding the different protonation states of the vanadate cofactor throughout the catalytic cycle—a central issue in the mechanism—have to be addressed theoretically. Reports on this subject have been published in recent years for chlorine and bromine<sup>26–31</sup> but not for iodine. The features that confer halide selectivity remain as yet unexplained. The nature of the species “X<sup>+</sup>” that ultimately halogenates organic compounds is an unanswered question. Although on a kinetic and structural basis it was considered unlikely that the halide-binding sites were found at the vanadium center,<sup>32,33</sup> recent experimental work<sup>26</sup> suggests otherwise. The specificity for halogenation of organic substrates is also an as yet unsolved question. Recent studies have shown specificity in bromination of cyclic molecules by VBrPOs,<sup>15,17,18</sup> but other results point to a lack of selectivity,<sup>34</sup> which has been interpreted to mean that the “Br<sup>+</sup>” intermediate was freely diffusible to facilitate bromination outside the active site.<sup>35</sup>

In this contribution, we focus on the iodoperoxidase VIPO enzyme identified in *L. digitata*.<sup>16</sup> On the basis of a reliable three-dimensional (3D) model of the whole protein and by means of a theoretical combined approach that uses quantum

calculations and structural modeling along with Poisson–Boltzmann (PB) electrostatic potentials and protein surface analyses, we address the following issues: (1) The active site of VIPO is compared to the sites of VCIPOs and VBrPOs with known structures to identify differences. (2) The topography of entrances to the active site cavity in the protein surfaces of VHPOs are compared, highlighting putative distinctive features in VIPO provided by the PB electrostatic potential. (3) Characterization of the vanadate cofactor and its protonation states throughout the catalytic cycle is explored on the basis of quantum calculations and 3D modeling of the active site. Results point to a specific protonation of the iodine-bound cofactor assisted by a nearby histidine, a step not proposed before. (4) Iodination reactions of several organic compounds selected to account for representative volatile and nonvolatile iodocarbons are thermodynamically studied at high-level *ab initio* correlated calculations. Free energies of reactions with the three possible iodinating species HOI, I<sub>2</sub>, and I<sub>3</sub><sup>−</sup> are calculated. Results indicate that only hypoiodous acid give clearly exergonic iodination of organic substrates.

## Methods

The 624-amino acid sequence of the vanadium peroxidase (VIPO) purified from *L. digitata*<sup>16</sup> deposited in the Peroxi-Base database<sup>36</sup> (entry 4072, UnitProtKB: Q4LDE6) was utilized to generate a model structure using the Swiss-model homology-modeling server.<sup>37</sup> The model was constructed from the X-ray structure of *A. nodosum* VBrPO<sup>23</sup> as a template and includes residues 66–623 (coordinates in PDB format and Figure S1 in the Supporting Information). Sequence identity between VIPO and VBrPO was 57.3%, and their structural superposition gave a RMSD for backbone atoms of 0.26 Å. A geometry obtained in quantum calculations for vanadate bonded to an imidazole ring was inserted in the VIPO model structure to fit the His555 side chain. Insertion of heterogroups and structure analyses were performed with Chimera 1.3.<sup>38</sup>

Besides the modeled structure of VIPO, the following crystal structures of VHPOs were used for comparison: resting forms of native (PDB code 1IDQ<sup>21</sup>) and recombinant (PDB code 1VNI<sup>22</sup>) VCIPO from *C. inaequalis*, its peroxide form VCIPO (PDB code 1IDU<sup>21</sup>), and its resting form of VBrPO from *A. nodosum* (PDB code 1QI9<sup>23</sup>). Solvent-excluded molecular surfaces for the five structures were obtained for a 1.4-Å-radius probe sphere and rendered with PyMOL 1.2.<sup>39</sup> Amino acid contributions to accessible surface areas and solvent exposure percentages were computed with Arvomol<sup>40</sup> and SurfRace.<sup>41</sup> Poisson–Boltzmann (PB) electrostatic potentials were obtained with APBS 1.2.1,<sup>42</sup> assigning AMBER99 charges<sup>43</sup> and atomic radii with PDB2PQR<sup>44</sup> to all the atoms including hydrogens added and optimized with this program. PB potentials were obtained at ~0.5 Å grid spacings around the more than 8000 atoms of which these proteins are composed by solving the nonlinear PB equation<sup>45</sup> in single-point multigrid calculations at meshes of 225 × 193 × 225 points at 298.15 K, 0.150 M ionic strength, and dielectric constants of 4 for proteins and 78.54 for water. Output meshes were processed in scalar

OpenDX format with PyMOL 1.2. PB potential values are given in units of  $kT/e$  ( $k$ , Boltzmann's constant and  $e$ , unit charge;  $1 kT/e = 2.48 \text{ kJ mol}^{-1}$  at 298.15 K). Since no AMBER parameters exist for vanadate, atomic charges were obtained at separate B3LYP/cc-pVTZ calculations to produce charges fit to the quantum electrostatic potential according to the CHelpG scheme.<sup>46</sup> An atomic radius of 1.6612 Å for oxygen (AMBER value for phosphate) and 2.0 Å for vanadium were assumed for vanadate.

Structures of vanadium cofactors at distinct protonation states throughout the catalytic cycle of VIPO were optimized in quantum calculations with the B3LYP hybrid functional and cc-pVTZ basis sets upon using an imidazole ring to represent the His555 side chain. Harmonic vibrational frequencies were then computed at the B3LYP geometries. The cc-pVTZ basis set for vanadium atom was taken from the basis set library by Balabanov and Peterson for transition elements,<sup>47</sup> while an equivalent valence-only basis set was developed for the iodine atom using a shape-consistent averaged relativistic effective potential (AREP)<sup>48</sup> to replace the 46-electron core.<sup>49</sup> This pseudopotential formalism has been shown to account for relativistic effects when used with properly optimized basis sets.<sup>50</sup> The cc-pVTZ basis set for iodine was generated following the method prescribed by Martin and Sundermann to construct correlated consistent basis sets for relativistic effective core potentials<sup>51</sup> using MOLPRO2006.<sup>52</sup> This AREP-optimized basis set (Table S1 in the Supporting Information) was tested in benchmark calculations on molecules containing iodine (for an illustrative example of its reliable performance, see Table 3 below). Full geometry optimizations using analytic gradients without symmetry constraints were performed and frequencies analyzed to characterize minima. Environmental effects were accounted for by computing Polarizable Continuum Model (PCM) energies with three dielectric constants:  $\epsilon = 4$  to simulate protein interiors,<sup>42</sup>  $\epsilon = 40$  to simulate charge–charge interactions in protein active sites as used before in quantum calculations on VBrPO,<sup>29,30</sup> and  $\epsilon = 78.39$  for an aqueous medium.

With the aim of thermodynamically studying iodination reactions of organic substrates, we selected the following iodocarbons: CH<sub>3</sub>I, CH<sub>2</sub>I<sub>2</sub>, and iodopropene isomers (CHI=CH–CH<sub>3</sub>, CH<sub>2</sub>=CI–CH<sub>3</sub>, and CH<sub>2</sub>=CH–CH<sub>2</sub>I) to represent volatile iodocarbons and CH<sub>2</sub>ICHO, CH<sub>2</sub>ICOOH, and iodophenol isomers to represent nonvolatile iodocarbons. The corresponding reactions of the possible iodinating species HOI, I<sub>2</sub>, and I<sub>3</sub><sup>−</sup> with methane, propene, acetaldehyde, acetic acid, and phenol to yield iodocarbons and byproducts H<sub>2</sub>O, HI, and I<sup>−</sup> were studied by means of *ab initio* calculations. Free energies were computed at 298.15 K as  $\Delta_R G^0_{298} = \Delta_R H^0_{298} - T \Delta_R S^0_{298}$  from enthalpies of formation  $\Delta_f H^0_{298}$  and absolute entropies  $S^0_{298}$  obtained with aug-cc-pVTZ basis sets (an AREP-optimized aug-cc-pVTZ set was constructed for iodine: see Table S1 in the Supporting Information). Geometries and vibrational frequencies to compute zero-point energies (ZPE) and thermal corrections were obtained at MP2 calculations. CCSD(T) energies were also computed at MP2 geometries. ZPE-corrected  $\Delta_f H^0_0$  values were first calculated at 0 K from known enthalpies



of formation of isolated atoms, as suggested by Curtiss et al.<sup>53</sup> for the set of molecules (A)  $\text{H}_2\text{O}$ ,  $\text{CH}_4$ ,  $\text{I}_2$ ,  $\text{HI}$ ,  $\text{HOI}$ ,  $\text{CH}_2=\text{CH}-\text{CH}_3$ ,  $\text{CH}_3\text{CHO}$ , and  $\text{CH}_3\text{COOH}$ .  $\Delta_f H^0_0$  values for the set of molecules (B)  $\text{CH}_3\text{I}$  and  $\text{CH}_2\text{I}_2$  were obtained from isogyric reactions  $\text{CH}_4 + \text{IH} \rightarrow (\text{B}) + \text{H}_2$ , while those for (C) the rest of the iodocarbons,  $\Delta_f H^0_0$ , were obtained from isodesmic reactions  $\text{substrate} + \text{CH}_3\text{I} \rightarrow (\text{C}) + \text{CH}_4$ . Reaction 3 was used for  $\text{I}_3^-$ .  $\Delta_f H^0_{298}$  values were then calculated by correction to  $\Delta_f H^0_0$  using atomic  $H^0_{298} - H^0_0$  thermal corrections from NIST-JANAF data<sup>54</sup> for molecules in set A and MP2 values for sets B and C. MP2 results for  $S^0_{298}$  were used in all cases except  $\text{I}^-$ , for which the experimental value was taken. Thermodynamical computed data and experimental values where available are gathered in Table S2 in the Supporting Information. All the calculations to obtain geometries, energies, frequencies, and PCM results were performed with Gaussian 03.<sup>55</sup>

## Results and Discussion

**Active Site of Vanadium Haloperoxidases.** We start addressing the reliability of the model structure of VIPO used in this work. Homology modeling, the approach followed to obtain the model structure, is currently considered the method of choice to predict the protein structure if the target protein has  $\sim 50\%$  sequence identity with a template protein.<sup>37,56</sup> Estimating the accuracy of homology-modeled structures has been an issue thoroughly studied for more than 20 years. During the past decade, blind tests such as those provided by the CASP (Critical Assessment of protein Structure Prediction) experiments have permitted the objective evaluation of the reliability of protein modeling methods by examining the quality of predictions. It has been demonstrated that the core atoms of protein models sharing 50% sequence identity with their templates deviate by RMS  $\sim 1.0$  Å from crystal structures.<sup>56</sup> Given the typical resolution of X-ray protein geometries, this deviation is more than acceptable. What is indeed more important here is that, if one is dealing with a family of proteins in which the function is maintained, as it is the case for VHPOs, binding and active sites are found to show even less deviation, as evolution tends to alter those sites rather conservatively.<sup>37,56</sup>

Most of the residues in active sites of VCIPOs and VBrPOs are conserved in *L. digitata* VIPO.<sup>16</sup> Superposition of the VIPO model structure with available crystal structures of *C. inaequalis* VCIPOs<sup>21,22</sup> and *A. nodosum* VBrPO<sup>23</sup> shows a remarkable fit of residues within 4 Å around vanadate (Figure 1A). Given that VBrPO was used as a template to model VIPO and that these proteins share 57% sequence identity, the near coincidence between their active sites is the expected result. However, neither of the resting VCIPO structures was used to model VIPO; hence, the good agreement between their active sites lends additional support to the predicted geometry of VIPO active site. Since the entry channel leading to the active site seems to play a crucial role in fine-tuning the activity of VHPOs (see the next subsection), this structural region must be also reliably predicted. Figure 1B shows the comparison between structural sections around the entry channel for the resting form of *C. inaequalis* native VCIPO<sup>21</sup> and VIPO (the comparison

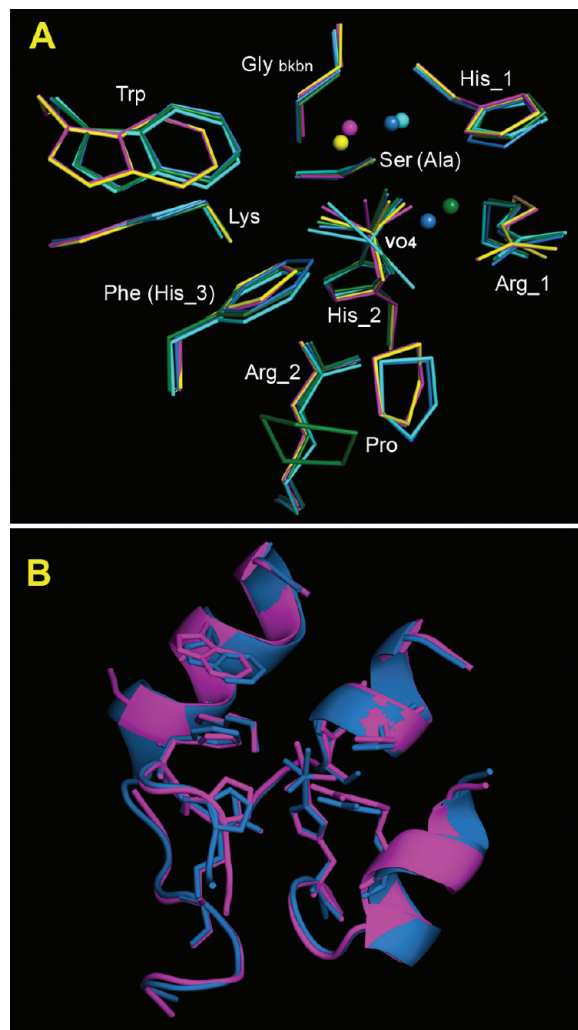
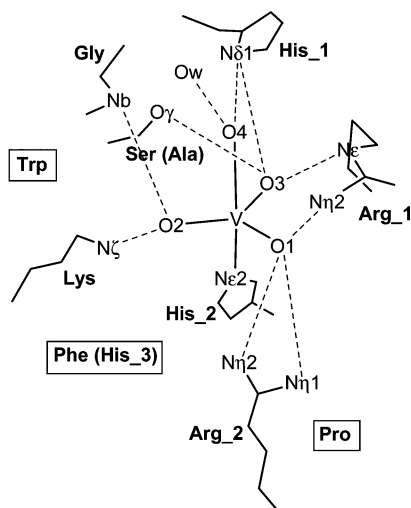


**Figure 1.** (A) Site defined by residues within a 4 Å radius around vanadate in crystal structures of two resting forms of VCIPOs (1IDQ, deep blue; 1VNI, green), peroxo form of VCIPO (1IDU, cyan), resting form of VBrPO (1QI9, yellow), and model structure of VIPO (magenta). Spheres represent water molecules. Apart from the glycine backbone, only side chains are shown. Residue numbering is given in Scheme 1. (B) Structural region around the entry channel to the active site in the crystal structure of resting form of VCIPO (1IDQ, blue) and model structure of VIPO (magenta). Sticks represent residues at the active site. Arrangements depicted in A and B result from superposing the whole proteins without constraining fit in the regions displayed.

with the template VBrPO yields a nearly indistinguishable superposition). It is seen that not only  $\alpha$  helices but also coil segments in this region are in a rather satisfactory agreement. The good match of conformation around this entry for the three VHPOs gives thus a sound basis for comparing its local surface topography, as discussed below. It must be stressed that Figure 1 was produced upon superposing the proteins to fit their whole structures, not the displayed regions alone.

On the other side, the close agreement between resting and peroxide forms of VCIPO indicates that the catalytic activity is carried out without noticeable structural changes at the active site. Vanadium is coordinated to the protein by a single axial His<sub>2</sub> ligand in a trigonal bipyramidal

**Scheme 1.** Schematic Drawing of Residues in the Active Site of Vanadium Haloperoxidases VHPOs (Figure 1), Atom Labeling and Residue Numbers in the Corresponding Sequences of H = Cl, Br, and I Enzymes<sup>a</sup>



	VCIPO	VBrPO	VIPO
Arg_1	490	480	549
His_1	404	418	483
Gly	403	417	482
Ser (Ala)	S402	S416	A481
Trp	350	338	400
Lys	353	341	403
Phe (His_3)	F397	H411	H476
Arg_2	360	349	411
Pro	395	409	474
His_2	496	486	555

<sup>a</sup> Amino acid atoms at intermolecular distances from vanadate oxygens shorter than 3.5 Å (dashed lines) are labeled. Nb is glycine backbone nitrogen, and Ow is water oxygen. Names inside boxes indicate residues not directly interacting with vanadate.

geometry, while oxygens of vanadate are hydrogen-bonded to Arg\_1, His\_1, Lys, Arg\_2, side chains, and the Gly backbone (Scheme 1). The spatial coincidence of these residues in all VHPOs demonstrates that they define a rigid scaffold setting a hydrogen bond network around vanadate regardless of the halogen specificity. However, some differences are noticed. As it was observed before,<sup>16</sup> VIPO has an alanine at a position occupied by serine in other haloperoxidases. It has been noted that this substitution, which results in the loss of one of the hydrogen bonds of vanadate, could be related with the inability of VIPO to oxidize bromide or chloride.<sup>16</sup> VBrPO and VIPO have histidine substituting phenylalanine in VCIPO at a location where no direct interaction with the vanadium cofactor is possible. It was conjectured that, whereas Phe397 in VCIPO might take part in halide binding through its aromatic ring,<sup>17,57</sup> His411 in VBrPO could participate in proton transfer during the enzymatic reaction,<sup>15,18</sup> though this role was not specifically elucidated. We propose in this work that His476 (VIPO numbering) should in fact participate in a water-assisted proton transfer to the apical oxygen bonded to iodine before releasing hypoiodous acid (see below). Two other differences that have apparently gone as yet unnoticed concern the locations of Trp and Pro, residues conserved in

VHPOs not interacting with vanadate. Trp and Pro show structural displacements between VCIPO on one side and VBrPO/VIPO on the other side, particularly Pro in recombinant *C. inaequalis* VCIPO.<sup>22</sup> Since halides are known to bind to hydrophobic pockets (apart from basic residues)<sup>16,18</sup> and it seems unlikely that halide specificity, an as yet unsolved question, could arise from the rigid scaffold, it seems reasonable to think of Trp and Pro besides Phe (His\_3) as residues involved in halide selectivity. We point in the next subsection to the topography of the active site surface and the local electrostatic potential as properties displaying differentiated features in this regard.

In contrast to other haloperoxidases which function as redox catalysts, the vanadium atom in VHPOs remains in the (v) oxidation state throughout the catalytic cycle; hence its role is to act as a Lewis acid in the activation of the primary oxidant H<sub>2</sub>O<sub>2</sub>.<sup>21–24</sup> Excluding the largely distorted geometry of the peroxo form, vanadate groups differ significantly even though His\_2 imidazole rings overlap when VHPO's structures are superposed (Figure 1). Given that the resolution of the available experimental structures does not allow solving hydrogens and the uncertainty of X-ray derived bond distances precludes unambiguous assignments, the protonation states of vanadate have to be theoretically deduced as was done before for VCIPO and VBrPO<sup>27–31</sup> and is reported here for VIPO. Nevertheless, vanadate bond lengths in crystal geometries hint at differences even between both resting forms of VCIPO. As shown below, V–O bond lengths of about 1.5–1.6 Å are typical of V=O double bonds, while lengths longer than 1.8 Å indicate V–OH bonds. All the equatorial O–V bonds in resting forms of VCIPO and VBrPO have distances between 1.52 and 1.64 Å. However, apical O4–V lengths are 1.88 Å in VCIPO (1IDQ) and 1.77 Å in VBrPO, both values consistent with V–OH bonds, but 2.15 Å in VCIPO (1VNI) and 2.19 Å in the VIPO model, which suggests instead a V••OH<sub>2</sub> interaction (see below).

**Surfaces and Local Electrostatic Potential.** X-ray structures of VHPOs show that the vanadium-binding site is positioned at the bottom of a deep funnel-shaped channel.<sup>21–23</sup> Although the VIPO structure is a model and as such merely tentative, the evidence presented in the preceding subsection allows one to reasonably discuss features in the region around the entry channel in VCIPO, VBrPO, and VIPO on a similar footing. Comparison among molecular surfaces (Figure 2) reveals a different local topography in the funnel entrance. While VCIPO exhibits a narrow entrance which is besides partially buried, VBrPO and VIPO display open, wider entrances, much greater in the latter. These differences become striking when one compares surface contributions from residues in the active site (Figure 3). All VHPOs have Ser(Ala) and Lys completely buried, while the bottom surface is made of Arg\_2 and His\_2 contributions. Arg\_1, His\_1, and Gly contribute significantly to the pocket wall surface, but as the cleft entrance is deeper in VCIPO, their surfaces are barely accessible from outside (Figure 3A). On the contrary, Arg\_1, Gly, and His\_1 surfaces form large outer patches around the channel entrance in VIPO (Figure 3B), though only Arg\_1 and His\_1 have surfaces accessible to

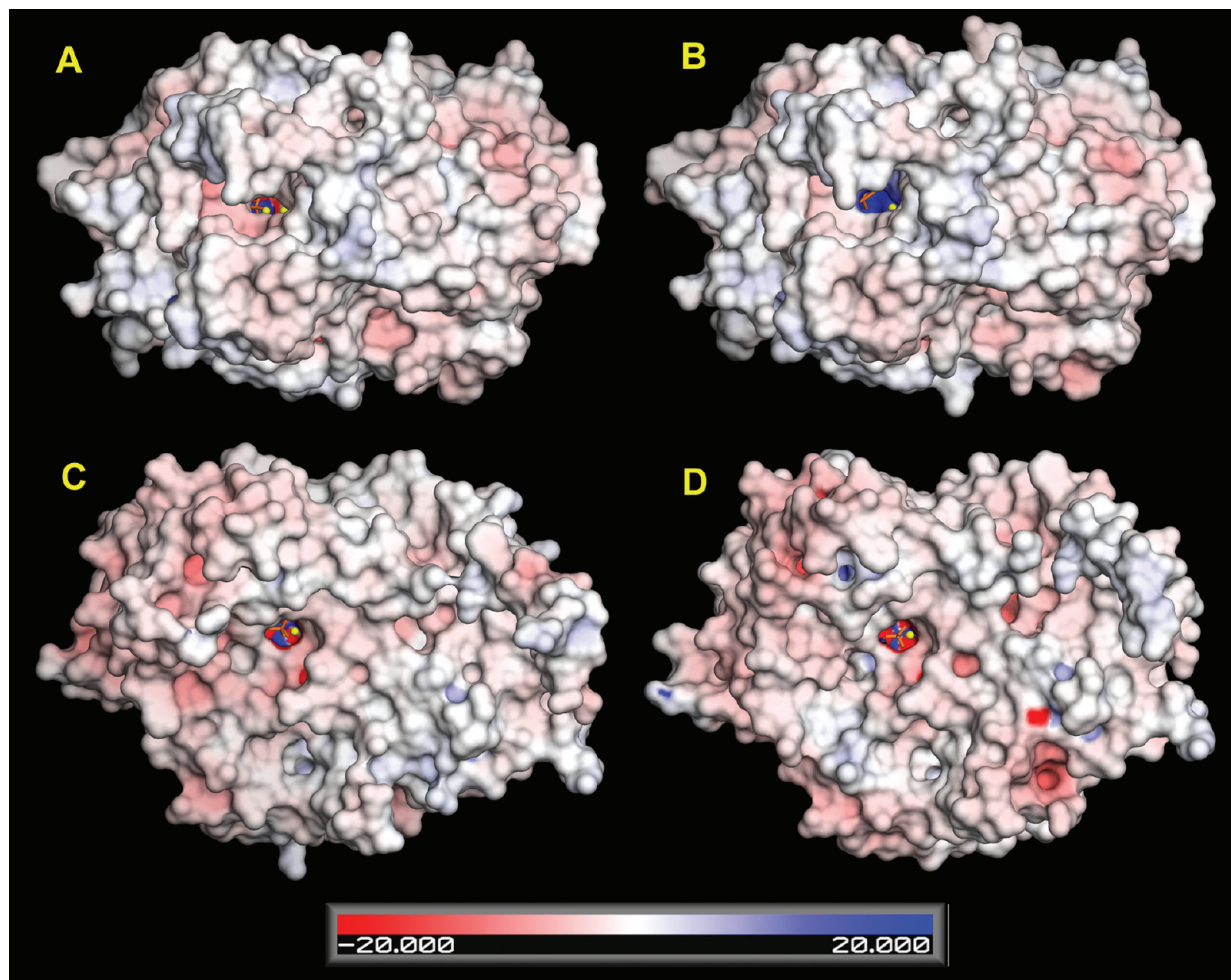


**Figure 2.** Poisson–Boltzmann electrostatic potential in the range  $-20$  to  $+20$  (units of  $kT/e$ ) mapped onto the molecular surface of vanadium haloperoxidases. Vanadate cofactor in the substrate binding pocket is drawn as orange sticks and water molecules as yellow spheres. (A) VCIPO (resting form, 1IDQ). (B) VCIPO (peroxo form, 1IDU). (C) VBrPO (1QI9). (D) VIPO.

the solvent (Table 1). More remarkable are the differences regarding residues found to be shifted in structural superpositions discussed above. In VCIPO, Pro and Phe form hydrophobic patches with similar surface areas at the entrance region inaccessible to solvent, and Trp is completely buried (Figure 3A, Table 1). In VIPO, His<sub>3</sub> and especially Pro and Trp are a great part of the surface around the cavity entrance forming a large hydrophobic area accessible to solvent (Figure 3B, Table 1). Comparing the small deep channel in VCIPO with the wide open cleft in VIPO, one could conclude that the access cavity topography is a clearly differentiated feature which might affect halide selectivity.

Another revealing difference appears when one analyzes a property that has been hitherto scarcely explored: the electrostatic potential. The dominance of acidic versus basic amino acids yields very large negative total electric charges in these enzymes:  $-26e$  in VCIPO,  $-43e$  in VBrPO, and  $-45e$  in VIPO. Therefore, the electrostatic potential at their surfaces displays a predominantly negative character, more significant in VIPO or VBrPO than in VCIPO (Figure 2). However, in choosing a large range of values as that used to render Figure 2, the active site pocket shows a local electrostatic potential markedly stronger than any other region at the protein surface. Gathering four basic residues (Arg<sub>1</sub>, His<sub>1</sub>, Lys, and Arg<sub>2</sub>) and four electronegative vanadate

oxygens at the active site produces strong local electrostatic potentials at the pocket (Figure 4). Comparing these local potentials thus gives useful information that complements that provided by local topography. Note that the three resting forms show at the bottom of the pocket two negative regions, but whereas VCIPO has a positive area in the surface near Arg<sub>1</sub> and His<sub>1</sub> (Figure 4A), VBrPO displays there a neutral/negative domain (Figure 4C), and VIPO shows only a negative domain (Figure 4D). This surface patch turns out to be located just above Lys and Ser (Ala), both completely buried residues (Table 1). In the crystal structures of VHPOs, it is found that Ser402 is at a short distance from vanadate equatorial oxygens in VCIPO ( $O3 \cdots O_{\gamma}$  distance  $\sim 2.6$  Å; see Scheme 1), and Ser416 is farther apart in VBrPO ( $O3 \cdots O_{\gamma}$  distance  $\sim 2.9$  Å), whereas VIPO has alanine instead serine at that position. Since the scaffold around the cofactor is nearly identical in all VHPOs and the atomic charges used for vanadate to compute PB potentials in the three resting forms were exactly the same, the Ser/Ala change had to give rise to local differences in the electrostatic potential at the cavity.

Another factor of interest is the rather distinct depth of the substrate cleft. It must be stressed that all pockets displayed in Figure 4 correspond to the same clipping 20 Å depth from the outer surface. As discussed above with regard



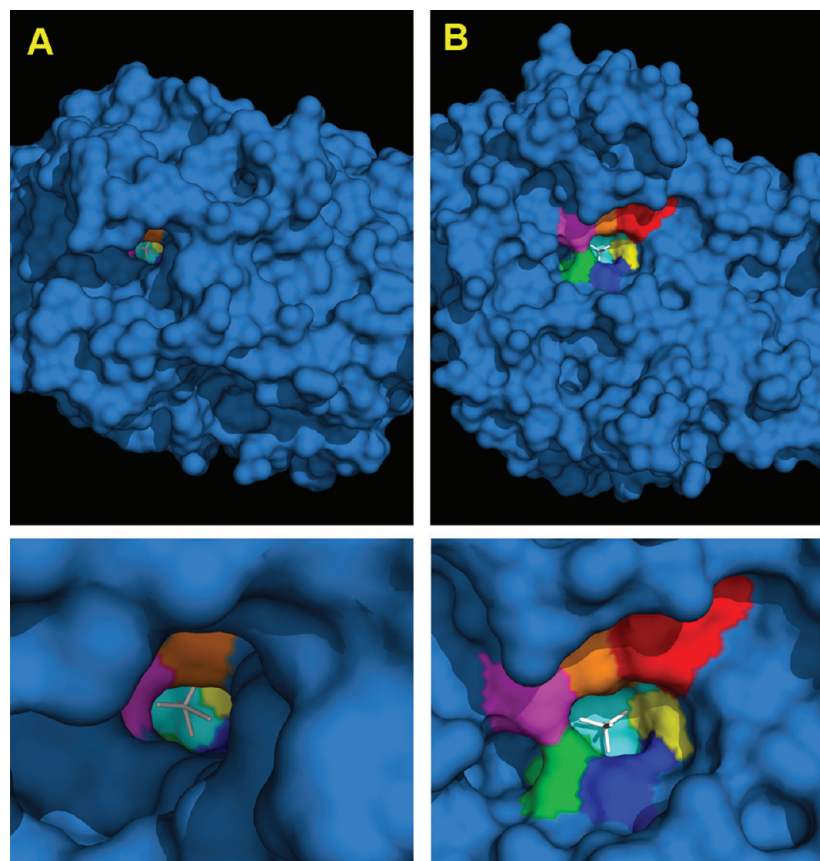


**Figure 3.** Molecular surface of VCIPO (A) and VIPO (B) showing contributions of residues in the active site. Top: general views of the protein surface. Bottom: closeup views of the entrance to the substrate channel. Vanadate cofactor drawn as white sticks. Bottom of the pocket colored cyan and residue contributions colored as follows: Arg\_1, green; His\_1, marine blue; Gly, yellow; Trp, red; Phe (His\_3), orange; and Pro, magenta. Residue numbering in Scheme 1.

**Table 1.** Surface Areas and Solvent-Exposure Percentages (In Parentheses) of Residues at the Active Site in Vanadium Haloperoxidases<sup>a</sup>

residue	VCIPO resting (1IDQ)	VCIPO peroxo (1IDU)	VBrPO resting (1QI9)	VIPO resting (Model)
Arg_1	8.7 (0.0)	11.5 (0.0)	32.8 (3.4)	39.2 (5.9)
His_1	29.8 (0.0)	23.4 (0.0)	37.1 (0.4)	36.3 (6.3)
Gly	13.3 (0.0)	15.5 (0.0)	17.8 (0.0)	18.8 (0.0)
Ser (Ala)	0.0 (0.0)	0.0 (0.0)	0.0 (0.0)	0.0 (0.0)
Trp	12.1 (0.6)	10.3 (0.6)	37.3 (4.5)	65.2 (10.0)
Lys	2.8 (0.0)	3.5 (0.0)	2.4 (0.0)	2.6 (0.0)
Phe (His_3)	26.3 (1.7)	26.5 (2.7)	23.9 (2.2)	39.6 (4.4)
Arg_2	27.3 (3.1)	29.3 (2.5)	21.7 (2.2)	20.0 (1.5)
Pro	26.4 (2.3)	29.8 (4.2)	46.2 (14.5)	48.0 (15.0)
His_2	12.5 (0.9)	14.7 (0.9)	12.1 (0.0)	12.4 (0.0)

<sup>a</sup> Areas in Å<sup>2</sup>. Residue labels in Scheme 1.

to the topography of cavity entrances, most of the residues in VCIPO lie under the outer surface (Figure 4A), whereas in VBrPO and especially VIPO, the outermost part of the cavity merges with the external protein surface (Figure 4C and D). Note finally that, as far as we chose the activated peroxo form of vanadate to represent the halide binding stage in the catalytic cycle and this corresponds to a positive charge of the cofactor (see next subsection), the peroxo form of VCIPO shows a strongly positive electrostatic potential at the active site which covers nearly all the pocket surface (Figure 4B).

### Vanadate Cofactor Throughout the Catalytic Cycle.

The protonation state of oxygen atoms of the vanadate cofactor is a key issue in elucidating the catalytic activity of vanadium haloperoxidases. Proposals on their mechanism derived from crystal structures<sup>21–26</sup> have been recently complemented by computational studies,<sup>27–31,58,59</sup> which has led to a better understanding of the catalytic properties of chlorine and bromine peroxidases. By using quantum calculations as explained in the Methods, we address now the theoretical analysis of the catalytic cycle of iodoperoxidase focusing on hitherto less explored details regarding the binding of iodide and the final release of hypoiodous acid.

X-ray structures show for vanadate equatorial O–V bond lengths ranging from 1.60 to 1.64 Å in VCIPO and between 1.52 and 1.60 Å in VBrPO. According to the evidence provided by previous quantum calculations<sup>27–31</sup> and in agreement with our results (Figure 5), these bond lengths may suggest that equatorial oxygen atoms are deprotonated in resting states of VHPOs. One should recall that these oxygens are stabilized by hydrogen bonds in the active site that anchor the cofactor at the protein (Scheme 1). As noted above, more noteworthy differences are found for apical oxygens even between both resting forms of VCIPO, with O–V bond lengths of 1.88 and 2.15 Å for 1IDQ and 1VNI structures, respectively. According to our calculations and in agreement with other reports,<sup>27–31,58,59</sup> such bond lengths may be ascribed to singly and doubly (as a water molecule)

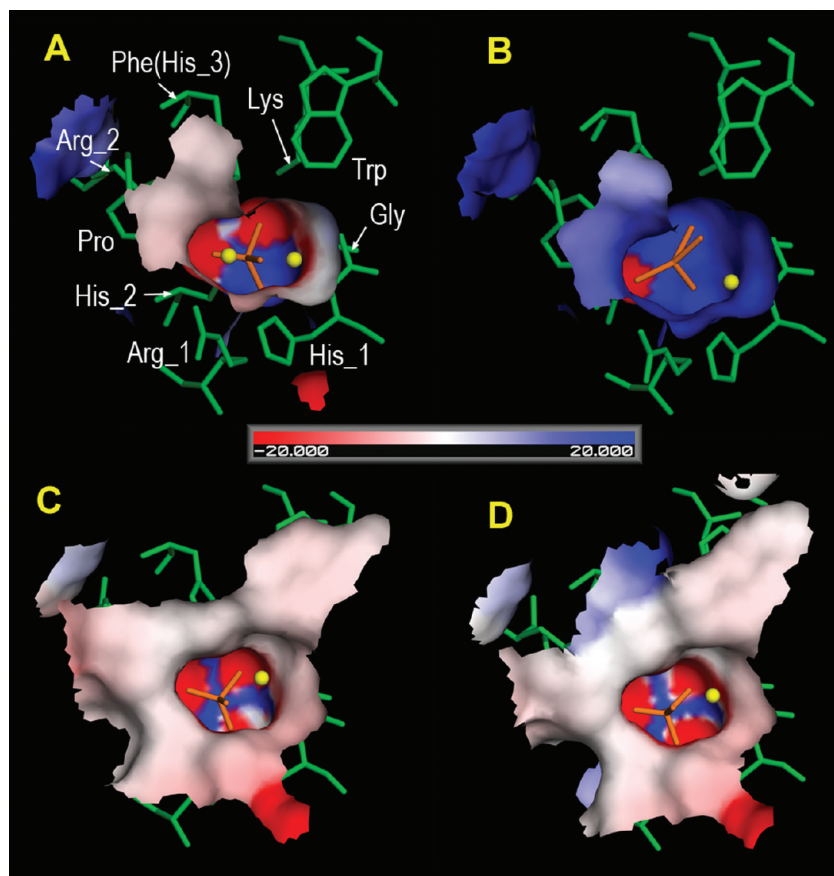


**Figure 4.** Poisson–Boltzmann electrostatic potential in the range  $-20$  to  $+20$  (units of  $kT/e$ ) mapped onto the molecular surface at the active site pocket. Surface clippings at  $20$  Å depth from the outer protein surface rendered at the same orientation. Residues drawn as green sticks, vanadate group as orange sticks, and water molecules as yellow spheres. Residue numbering in Scheme 1. (A) VCIPO (resting form, 1DQ). (B) VCIPO (peroxo form, 1DU). (C) VBrPO (1QI9). (D) VIPO.

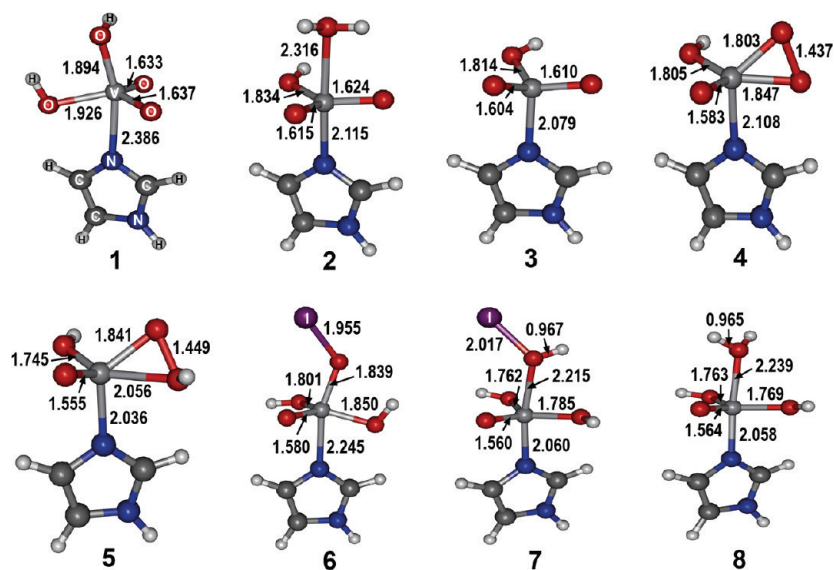


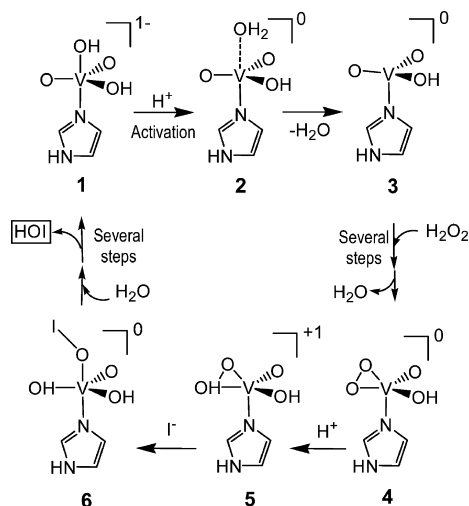
**Figure 5.** Optimized structures of model complexes involved in the catalytic cycle of VIPO. Distances in Ångströms.

protonated oxygen atoms, respectively (Figure 5). The apical O–V distance for VBrPO,  $1.77$  Å, suggests the presence of a hydroxyl group. Apical oxygen is also stabilized by hydrogen bonds with His\_1 and water molecules (Figure 1A, Scheme 1).

Recent experimental and theoretical studies have shown that the vanadate anion in resting states of VHPOs can be

described as an equilibrium between a structure with hydroxyl groups in equatorial and apical positions, **1** (structure numbers and bond lengths refer hereafter to Scheme 2 and Figure 5), and another structure with an apical water molecule and three equatorial oxo bonds.<sup>27,58–60</sup> A better description of observed  $^{51}\text{V}$  NMR chemical shifts and UV–vis spectra of VCIPO is indeed provided when the



**Scheme 2.** Catalytic Cycle for Vanadium Iodoperoxidase

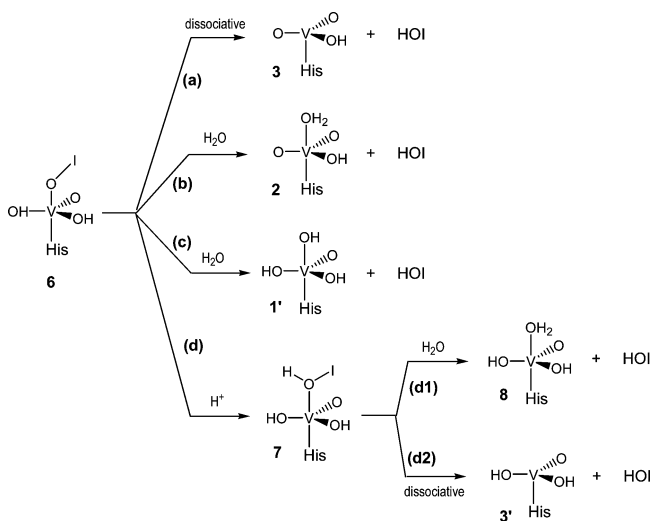
cofactor has apical water.<sup>31</sup> However, it must be noted that our calculations were unable to find optimized geometries of the isolated cofactor with unprotonated equatorial oxygens. This result, observed before in calculations with different functionals,<sup>28</sup> and the fact that X-ray distances seem to discard the presence of hydroxyl in the equatorial position, bring out the need of hydrogen bonds at those positions to stabilize the structure. It has been suggested that, in accordance with earlier kinetic studies on synthetic models that pointed out the role of protonation to render more labile oxo/hydroxo ligands of vanadium complexes,<sup>60</sup> the first stage of the catalytic cycle must be protonation of the anionic resting form,<sup>27,30</sup> a task presumably accomplished by His<sub>1</sub>.<sup>17,18</sup> In agreement with this suggestion, we found that the protonation of **1** forms a neutral complex with apical water and equatorial hydroxyl, **2**. Note that, in the process **1** → **2**, the V–N bond length shortens and the opposite happens for the apical O–V value, indicating that this bond weakens in the resting state as a preceding step to the subsequent release of water.

In the study of Zampella et al. on the catalytic activity of VBrPO with DFT calculations performed on a model isolated imidazole–vanadate complex,<sup>30</sup> **2** was assumed as initial structure to obtain the peroxo state of the cofactor. Our calculations (carried out following a different methodology) agree with most of their suggestions and add some supplementary details to the catalytic processes illustrated in Scheme 2 for the VIPO case. In brief, our results predict that the release of the apical water molecule from **2** with the formation of **3** is exoergonic:  $\Delta G = -4.1$  in the gas phase and  $\sim -10$  kcal mol<sup>-1</sup> when solvent is incorporated (Table 2). Species **3** is a tetrahedral intermediate with only three oxygen atoms and a short V–N bond length. It is accepted that, in the next catalytic step, the incoming hydrogen peroxide displaces the apical water and one equatorial oxygen, leading to the neutral peroxo form **4**.<sup>17,18,27,29,30</sup> Peroxide is thus coordinated in a side-on manner in the equatorial plane, distorting the vanadium cofactor and producing a square-based pyramidal oxo-peroxo–vanadium(v) intermediate in the peroxo form of VCIPO.<sup>21</sup> It is interesting to mention that our quantum geometry for the isolated intermediate, **4**, is rather similar

**Table 2.** Standard Free Energies at 298 K,  $\Delta_R G^\circ$ , for Processes Involved in the Catalytic Cycle of VIPO in the Gas Phase ( $\epsilon = 1$ ) and Obtained in PCM Calculations with  $\epsilon = 4, 40$ , and 78.39<sup>a</sup>

process <sup>b</sup>	$\Delta_R G^\circ$ ( $\epsilon = 1$ )	$\Delta_R G^\circ$ ( $\epsilon = 4$ )	$\Delta_R G^\circ$ ( $\epsilon = 40$ )	$\Delta_R G^\circ$ ( $\epsilon = 78.39$ )
<b>2</b> → <b>3</b> + H <sub>2</sub> O	-4.11	-8.41	-10.5	-10.6
<b>5</b> + I <sup>-</sup> → <b>6</b>	-146	-62.6	-37.1	-35.8
(a) <b>6</b> → <b>3</b> + HOI	2.05	-7.25	-11.4	-11.7
(b) <b>6</b> + H <sub>2</sub> O → <b>2</b> + HOI	6.16	1.16	-0.96	-1.09
(c) <b>6</b> + H <sub>2</sub> O → <b>1'</b> + HOI	1.34	-0.39	-1.42	-1.49
(d1) <b>7</b> + H <sub>2</sub> O → <b>8</b> + HOI	-3.98	-5.28	-5.26	-5.25
(d2) <b>7</b> → <b>3'</b> + HOI	-2.41	-8.21	-10.2	-10.3

<sup>a</sup> B3LYP/cc-pVTZ calculations. Values in kcal mol<sup>-1</sup>. <sup>b</sup> Labels refer to Schemes 2 and 3.

**Scheme 3.** Pathways to the Release of Hypoiodous Acid from Axially Coordinated Hypoiodite Intermediate **6**

to that of the cofactor in the X-ray structure (1IDU) of the peroxo form of VCIPO.<sup>21</sup>

This peroxo crystal structure shows that His<sub>1</sub> is no longer hydrogen-bonded while Lys makes direct contact with one peroxo oxygen atom (see Scheme 1). Experimental data<sup>26,60</sup> and theoretical studies<sup>27,29</sup> suggest that protonation of the peroxo moiety is a crucial factor in the activation of peroxo–vanadium complexes and further reaction with halide. Our calculations predict that protonation of **4** should in fact occur at the equatorial oxygen atom of the peroxo group, leading thus to structure **5**. It must be stressed that just this oxygen is hydrogen-bonded to Lys in the X-ray structure, which suggests that this amino acid might play a role in activating the bound peroxide. It is accepted that this protonation is an essential feature of the catalytic mechanism as far as it would increase the potential of the oxo-peroxo–vanadium(v) intermediate for further halide oxidation.<sup>18</sup> Replacement of Lys353 in VCIPO with alanine resulted in a considerably reduced catalytic efficiency, which led to the suggestion that the positively charged lysine should polarize the bound peroxide and hence favor nucleophilic attack by the substrate.<sup>61</sup>

The oxo-peroxo species **5** then oxidizes halide, the second substrate of the cycle, by two electrons forming thus an oxidized halogen that is formally at the X<sup>+</sup> oxidation state. However, detection or isolation of the oxidized halogen

intermediate is hampered due to its further reaction either with organic substrates (see below) or with a second  $\text{H}_2\text{O}_2$  molecule forming singlet  $\text{O}_2$ .<sup>10,11,15,17,18</sup> Therefore, details on completion of the catalytic cycle which entails releasing of the species “ $\text{X}^+$ ” and recovering of the initial resting form must rely exclusively on theoretical work. Previous DFT investigation on bromide<sup>29,30</sup> and our present computational study on iodide show that halide binding involves the remaining unprotonated peroxy oxygen atom. Our calculations predict that the reaction of iodide with **5** to form **6** is strongly exoergonic ( $-36 \text{ kcal mol}^{-1}$  in aqueous phase; Table 2). Geometry data for the hypiodite adduct **6** are in excellent agreement with the equivalent hypobromite structure obtained by Zampella et al.<sup>30</sup> except the axial  $\text{O}-\text{X}$  bond length, obviously longer for I ( $1.96 \text{ \AA}$ ) than for Br ( $1.86 \text{ \AA}$  in ref 30).

To close the catalytic cycle of VIPO, the axially coordinated hypiodite must be replaced by a water molecule (**6**  $\rightarrow$  **1** in Scheme 2), a process that can in principle occur according to distinct reaction channels illustrated in Scheme 3. We calculated  $\Delta G$  under different environment effects (Table 2) for these reactions, all of them involving release of HOI. A dissociative pathway (a) with the formation of **3** is only slightly endoergonic in the gas phase but becomes more favored as increasingly polar media are introduced. This result is similar to that obtained by Zampella et al.<sup>30</sup> for the analogous process with bromine, and also in agreement with this report, we were unable to find low-barrier transition states linking structures **6** and **3**. Direct reactions of **6** with a water molecule to recover resting forms, either **2** in pathway b or an alternative structure **1'** in pathway c, are predicted to be favored very little by our calculations. In agreement again with the bromine case,<sup>30</sup> no low-barrier transition states for these reactions have been found either for the iodine system. We obtained instead stable **6**–water complexes (stabilization energies greater than  $30 \text{ kcal mol}^{-1}$ ) with very strong hydrogen bonds between oxygens of water and vanadate. A similar result was found when a water molecule was introduced in the case of the dissociative pathway mentioned above.

A different possibility not considered before might be protonation of **6** in a similar way to the activation of **1** and **4**. A computational exploration of distinct possible products in pathway d yielded compound **7** as the most stable structure arising from protonating apical oxygen bonded to iodine. Final release of hypoiodous acid from **7** is predicted to be favored either by water displacing HOI, pathway d1, or by following the dissociative pathway d2, both processes becoming more exoergonic upon inclusion of environmental effects, although with little variation with the dielectric constant. Pathway d1 was found to be a barrierless process so that replacement of HOI by water would also be kinetically favored. Because adding a water molecule to **3'** yields **8**, deprotonations of this product allow recovery of initial vanadate structures, either **1** or **2**, in the resting state of the enzyme. We propose that the protonation of **6** and further deprotonation of **8** to close the catalytic cycle of VIPO might be assisted by His476 (His<sub>3</sub> in Scheme 1). This proposal should be supported by the location of the imidazole

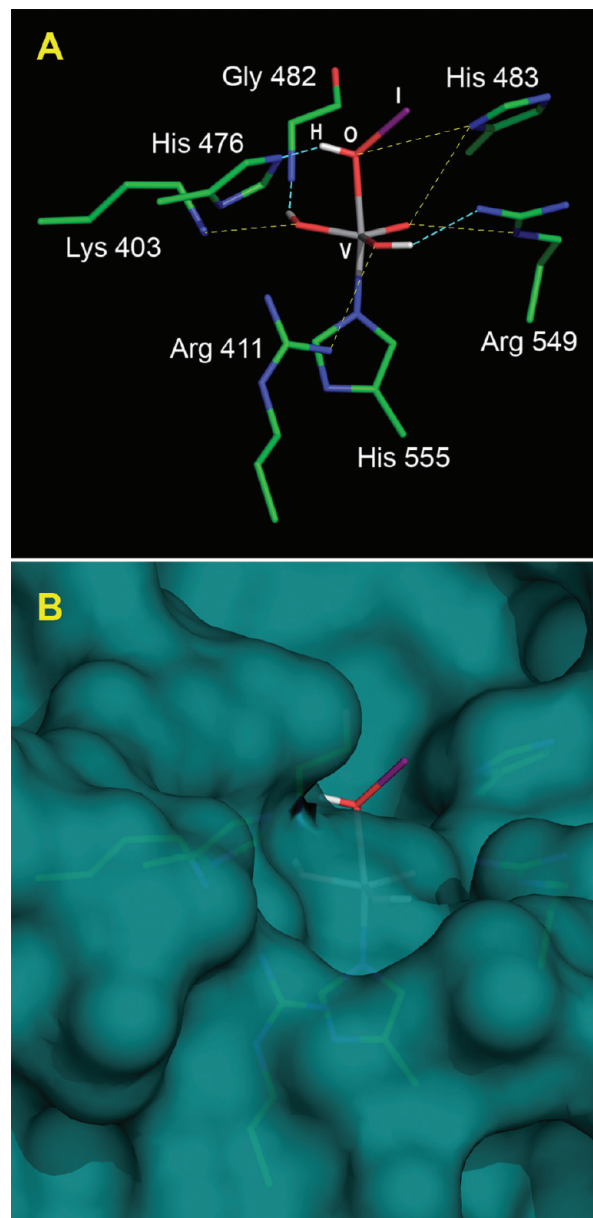


**Figure 6.** (A) Residues in the active site of VIPO interacting with HOI–vanadate complex **7**. Yellow dashed lines represent hydrogen bonds between non-hydrogen atoms. Cyan dashed lines represent hydrogen bonds involving hydrogen atoms in the quantum optimized geometry of **7**. (B) Close-up view of VIPO molecular surface at the entrance to the substrate channel rendered at the same orientation in A.

ring of this histidine with respect to the apical position of structure **6** or **7** (Figure 6). After inserting **7** in the active site of VIPO, the hydrogen bond network of VHPOs (Scheme 1) is essentially kept, with both hydrogen atoms in the equatorial position in the quantum geometries of vanadate forming  $\text{O}_2\text{--Nb}$  (Gly 482) and  $\text{O}_1\text{--N}\eta 2$  (Arg 549) hydrogen bonds (Figure 6A). In addition, we found that apical HOI is properly located to interact with His476. Moreover, exploratory calculations showed that internal rotation of the HOI moiety around the apical  $\text{O}-\text{V}$  bond is essentially barrierless (B3LYP/cc-pVTZ energies differ by a few tenths of a kilocalorie per mole), which suggests that the conformation of hypoiodous acid in the vanadate cofactor must be

determined by hindrance effects on the iodine atom arising from residues in the active site. In fact, the protein surface shows that the HOI group is positioned at the outer region of the cavity entrance with the bulky iodine atom positioned at the greater external part of the cleft (Figure 6B). Replacement by water and further release of hypoidous acid suggested by pathway d in Scheme 3 should be thus facilitated.

**Iodination Reactions with Organic Substrates.** If an organic substrate is present, it will react with the species “X<sup>+</sup>” generated in the mechanism producing a halogenated compound. Experimental studies indicated that hypohalous acid formed in the catalytic cycle of VHPOs acts as a halogenating agent such as HOX<sup>62</sup> or, in the case of bromide and iodide, as X<sub>3</sub><sup>−</sup>.<sup>32,63</sup> Reports on VBrPO activity suggest that the nature of the “Br<sup>+</sup>” intermediate either as enzyme-bound or as a freely diffusible species apparently depends on the type of organic substrate.<sup>15,62,64</sup> Although there is no direct evidence on the migration of HOBr from the VBrPO active site, a new fluorescence microscopy-based method will permit the monitoring of that process, shedding light on where halogenation of organic substrate actually occurs.<sup>65</sup> The apparent lack of organic substrate specificity in VBrPO was initially interpreted to mean that the enzyme produces a diffusible “Br<sup>+</sup>” species that could then carry out bromination reactions.<sup>15,18,34,35</sup> However, recent kinetics studies suggest that the active site channel would hold organic compounds (terpenes and lactones, mainly) in place.<sup>15,18</sup> The role of the site channel in substrate selectivity and the reason why some halogenated products predominate in one alga but not in another related alga with similar VHPO are still open questions.

With regard to iodoperoxidase, no studies on the iodination of organic substrates have been carried out yet. Recent competition experiments indicate that chlorine does not bind to *L. digitata* VIPO, whereas bromide does but in a nonproductive manner.<sup>16</sup> Given the close evolutionary relationship between VIPO and VBrPO, the specificity for iodide of the former led to conjecture that the ancestral VHPO enzyme in brown algae would have been a BrPO and that the loss of bromination in favor of iodination capability had given rise to a novel biochemical function.<sup>16</sup> This agrees with the recently proposed role of VIPO concerning the production of iodocarbons in kelps. On the one hand, these compounds have known microbial toxicity,<sup>11,19</sup> on the other, iodide accumulation acts as a potent inorganic antioxidant, and I<sup>−</sup> incorporated in iodocarbons would be easily regenerated by nucleophilic substitution with Cl<sup>−</sup>, Br<sup>−</sup>, or HO<sup>−</sup>.<sup>11</sup> Elucidating details on VIPO-catalyzed production of iodocarbons still needs much experimental work; hence, even conjecturing about that issue is obviously far beyond the scope of this work. We focus here on computing free energies of iodination reactions of common organic molecules by HOI, I<sub>2</sub>, and I<sub>3</sub><sup>−</sup>. We aim merely to provide the first thermodynamical information regarding the “I<sup>+</sup>” iodinating species. It is evident that solvent effects and species in solution different from those dealt with here had to be considered in further studies on iodination reactions associated with the catalytic activity of VIPO. We are currently

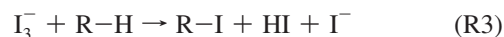
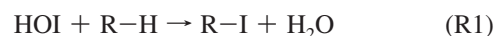
**Table 3.** Properties Computed with the aug-cc-pVTZ Basis Set (AREP-Optimized Set for Iodine Atom) for Iodine Species<sup>a</sup>

property	MP2 <sup>b</sup>	CCSD(T) <sup>b</sup>	theoretical	experimental
I <sub>2</sub>				
<i>r</i> <sub>e</sub>	2.662	2.690	2.683 <sup>c</sup>	2.666 <sup>d</sup>
<i>ω</i> <sub>e</sub>	226.2	211.6	215.8 <sup>c</sup>	214.5 <sup>d</sup>
<i>D</i> <sub>e</sub>	1.91	1.80	1.13 <sup>c</sup>	1.54 <sup>d</sup>
I <sup>−</sup>				
E.A.	3.21	3.15	2.74 <sup>e</sup>	3.06 <sup>f</sup>
I <sub>2</sub> + I <sup>−</sup> → I <sub>3</sub> <sup>−</sup> reaction				
Δ <sub>R</sub> <i>H</i> <sup>o</sup> <sub>0</sub>	−134.5	−124.6		−126 ± 6 <sup>g</sup>
I <sub>3</sub> <sup>−</sup>				
Δ <sub>f</sub> <i>H</i> <sup>o</sup> <sub>0</sub>	−257.0	−247.1		−248.5 <sup>g</sup>
Δ <sub>f</sub> <i>H</i> <sup>o</sup> <sub>298</sub>	−253.8	−243.9	171.3 <sup>e</sup>	−252 ± 6 <sup>g</sup>
Δ <sub>f</sub> <i>G</i> <sup>o</sup> <sub>298</sub>	−267.8	−257.9		−266 <sup>g</sup>
<i>r</i> <sub>e</sub>	2.936	2.967	3.002 <sup>h</sup>	
<i>ω</i> <sub>e</sub>	58.74 (Π <sub>u</sub> )	56.35	54.06, <sup>e</sup> 58.20 <sup>h</sup>	
	117.7 (Σ <sub>g</sub> )	111.2	106.5, <sup>e</sup> 107.3 <sup>h</sup>	112 <sup>i</sup>
	147.8 (Σ <sub>u</sub> )	136.7	145.1, <sup>e</sup> 139.6 <sup>h</sup>	139.6 <sup>i</sup>

<sup>a</sup> *r*<sub>e</sub>: bond length. *ω*<sub>e</sub>: harmonic vibrational frequencies. *D*<sub>e</sub>: dissociation energy. E.A.: electron affinity. Δ<sub>R</sub> *H*<sup>o</sup><sub>0</sub>: standard enthalpy of reaction at 0 K. Δ<sub>f</sub> *H*<sup>o</sup><sub>T</sub>: standard enthalpy of formation at *T* K. Δ<sub>f</sub> *G*<sup>o</sup><sub>298</sub>: standard Gibbs free energy of formation at 298 K. *r*<sub>e</sub> in eV, *ω*<sub>e</sub> in cm<sup>−1</sup>, *D*<sub>e</sub> and E.A. in eV, and Δ<sub>f</sub> *H*<sup>o</sup> and Δ<sub>f</sub> *G*<sup>o</sup> in kJ mol<sup>−1</sup>. <sup>b</sup> This work. <sup>c</sup> CCSD(T)/cc-pVTZ valence-only ECP/CPP calculations.<sup>51</sup> <sup>d</sup> Reference 66. <sup>e</sup> PW91/cc-pVTZ valence-only ECP calculations.<sup>67</sup> <sup>f</sup> Reference 54. <sup>g</sup> Reference 68. <sup>h</sup> QCISD(T)/TZ all-electron calculations.<sup>69</sup> <sup>i</sup> Reference 69.

undertaking this work, which will be the subject of forthcoming papers.

If R–H represents an organic compound, the iodination reactions studied are the following:



Before discussing Δ<sub>R</sub> *G*<sup>o</sup><sub>298</sub> values obtained as explained in the Methods, Table 3 presents a reliability test of our methodology (that concerns especially performance of the AREP/cc-pVTZ basis set for iodine) by displaying some molecular properties for iodine species related with I<sub>3</sub><sup>−</sup>. Gibbs free energies of iodination reactions are listed in Table 4. CH<sub>3</sub>I, CH<sub>2</sub>I<sub>2</sub>, and iodopropene were chosen to represent volatile iodocarbons while CH<sub>2</sub>ICOH, CH<sub>2</sub>ICOOH, and iodophenol were selected to represent nonvolatile compounds. Both methane derivatives are the most abundant alkyl iodides over oceans, and their release by phytoplankton and algae has been long known.<sup>1</sup> Propene and acetaldehyde iodinated derivatives were chosen, as it was found that they are major factors for regulating reactive halogen chemistry in the MBL.<sup>70</sup> Iodoacetic acid was proposed as one of the possible organic compounds identified in a recent experimental study on iodine speciation in rain and aerosols.<sup>71</sup> Finally, phenol is the side chain of tyrosine, an amino acid that plays a crucial role in biological processing of iodine in all living organisms.

Δ<sub>R</sub> *G*<sup>o</sup><sub>298</sub> values in Table 4 agree in predicting a markedly exoergonic iodination reaction with HOI in contrast to reactions with I<sub>2</sub> and I<sub>3</sub><sup>−</sup>, which are strongly endoergonic.



**Table 4.** Standard Free Energies at 298 K,  $\Delta_R G^\circ$ , for Iodination Reactions R1, R2, and R3<sup>a</sup>

R-H	R-I <sup>b</sup>	$\Delta_R G^\circ$ MP2			$\Delta_R G^\circ$ CCSD(T)		
		R1	R2	R3	R1	R2	R3
CH <sub>4</sub>	CH <sub>3</sub> I	-88.18	+47.95	+91.89	-84.34	+50.24	+100.5
CH <sub>4</sub>	CH <sub>2</sub> I <sub>2</sub>	-31.26	+104.9	+148.8	-17.16	+117.4	+167.7
CH <sub>2</sub> =CH-CH <sub>3</sub>	CH <sub>2</sub> =CI-CH <sub>3</sub>	-97.64	+38.50	+82.43	-129.3	+5.29	+55.55
CH <sub>2</sub> =CH-CH <sub>3</sub>	Z- CHI=CH-CH <sub>3</sub>	-93.36	+42.77	+86.62	-126.7	+7.88	+58.14
CH <sub>2</sub> =CH-CH <sub>3</sub>	E- CHI=CH-CH <sub>3</sub>	-89.85	+46.28	+90.21	-123.7	+10.85	+61.11
CH <sub>2</sub> =CH-CH <sub>3</sub>	(g)- CH <sub>2</sub> =CH-CH <sub>2</sub> I	-89.06	+47.07	+91.00	-124.5	+10.11	+60.37
CH <sub>2</sub> =CH-CH <sub>3</sub>	(e)- CH <sub>2</sub> =CH-CH <sub>2</sub> I	-83.88	+52.25	+96.18	-118.9	+15.67	+65.93
CH <sub>3</sub> -CHO	(g)- CH <sub>2</sub> I-CHO	-55.59	+80.54	+124.5	-117.1	+17.53	+67.79
CH <sub>3</sub> -CHO	(e)- CH <sub>2</sub> I-CHO	-49.47	+86.66	+130.6	-110.9	+23.71	+73.97
CH <sub>3</sub> -COOH	(g)- CH <sub>2</sub> I-COOH	-16.44	+119.7	+163.6	-117.0	+17.59	+67.85
CH <sub>3</sub> -COOH	(e)- CH <sub>2</sub> I-COOH	-14.68	+121.5	+165.4	-115.1	+19.47	+69.73
PhOH	<i>o</i> -trans-IPhOH	-73.92	+62.21	+106.1	-77.40	+57.18	+107.4
PhOH	<i>m</i> -trans-IPhOH	-76.35	+59.78	+94.81	-79.81	+54.77	+105.0
PhOH	<i>p</i> -IPhOH	-75.66	+60.48	+104.4	-79.91	+54.68	+104.9
PhOH	<i>m</i> -cis-IPhOH	-76.73	+59.40	+103.3	-80.15	+54.43	+104.9
PhOH	<i>o</i> -cis-IPhOH	-85.52	+50.61	+94.54	-88.68	+45.90	+96.16

<sup>a</sup> Values in kJ mol<sup>-1</sup>. <sup>b</sup> (g) and (e) indicate *gauche* and *eclipse* conformations, respectively. For CH<sub>2</sub>I-CHO and CH<sub>2</sub>I-COOH conformations, refer to the relative position of iodine atom and carbonyl oxygen.

Significant differences between MP2 and CCSD(T) results are noticed in some cases, especially for acetic acid and acetaldehyde reactions due to the rather distinct  $\Delta_f H^\circ_{298}$  values obtained for these molecules (Table S2 in the Supporting Information). This notwithstanding, MP2 and CCSD(T) results display similar trends for differences between reactions R1–R3. If one considers the magnitude of free energies in Table 4, the thermodynamical efficiency of HOI compared with the other iodinating reagents seems beyond question. Note besides that both methods also agree in predicting the small differences in favor of more stable isomers:  $\sim 3$  kJ mol<sup>-1</sup> for the *Z* isomer of CHI=CH-CH<sub>3</sub>,  $\sim 5$  kJ mol<sup>-1</sup> for the *gauche* conformations of both CH<sub>2</sub>=CH-CH<sub>2</sub>I and CH<sub>2</sub>ICHO, and  $\sim 2$  kJ mol<sup>-1</sup> for the *gauche* conformation of CH<sub>2</sub>ICOOH. MP2 and CCSD(T) energies agree again in distinguishing quantitatively the stability of iodophenol isomers: *o*-trans- is the less favored and *o*-cis- the more favored with a significant difference greater than 8 kJ mol<sup>-1</sup> with respect to the remaining isomers, a result that may be temptatively explained by the stabilizing effect associated with an intramolecular I $\cdots$ H–O hydrogen bond in this isomer.

## Conclusions

The active site of the structure modeled for VIPO superposes well with active sites of available crystal structures of chlorine and bromine VHPOs. The hydrogen bond network settled by residues defining the scaffold that anchors the vanadate cofactor is conserved in VIPO, except the position of Ser in VCIPO and VBrPO that is occupied by Ala in VIPO. Differences noticed in the spatial location of conserved Trp and Pro along with substitution of His for Phe (also present in VBrPO) are other distinctive structural features of the active site in VIPO.

Electrostatic potential at vanadium-binding site cavities of VHPOs is much stronger than at any other region of protein surfaces due to the presence of four electronegative oxygens of vanadate and four basic residues. However, small differences in the local electrostatic potential at the site

pockets reveal a negative domain in VIPO at a region where VCIPO and VBrPO have positive or neutral potentials. This region corresponds to the position of Ala in VIPO that substitutes Ser in the other VHPOs. Hence, we propose that this mutation might be associated with small changes of electrostatic potential related with binding iodine instead of the more electronegative bromine or chlorine.

Significant differences in the local topography of cavity entrances are found. VCIPO has a deep entrance with nearly buried large regions, whereas VIPO exhibits a great part of the surface around the cavity entrance accessible to the solvent. These differences affect especially hydrophobic patches corresponding to conserved Trp and Pro and the surface region of His476 that is largely exposed in VIPO, whereas it is nearly buried in VCIPO. The wide open cleft in VIPO opposite the small deep channel in VCIPO suggests that the topography of the access cavity leading to the active site might be a relevant factor regarding halide selectivity in these enzymes.

Quantum calculations were performed to obtain structures and energies of imidazole–vanadate complexes intended to model the cofactor throughout the catalytic cycle of VIPO. Stages corresponding to activation of the initial resting form, subsequent displacement of apical water and binding of hydrogen peroxide, protonation at the equatorial position to activate the peroxo form, and further oxidization of iodide with the binding of I at an apical position parallel those reported before for VBrPO with a different methodology. To close the catalytic cycle, a water molecule replaces axially coordinated hypoiodite recovering the initial resting form. We suggest a pathway consisting of protonation of apical oxygen bonded to iodine and further displacement of HOI by water either at a dissociative reaction or by direct replacement, both exoergonic processes. Inserting these intermediates at the VIPO structure indicates that His476 might assist this protonation, as it is properly located to interact with the apical OI group. Internal rotation of the resulting HOI around the apical O–V bond is found to be essentially free so that the HOI conformation should be

determined only by hindrance effects on the active site. The HOI group is located at the outer region of the cavity entrance with the bulky iodine atom positioned at a great external cleft region which facilitates release of hypoiodous acid.

Gibbs free energies of iodination reactions of common organic molecules by HOI, I<sub>2</sub>, and I<sub>3</sub><sup>−</sup>, the three iodinating "I<sup>+</sup>" reagents released by the catalytic activity of VIPO, were obtained in *ab initio* MP2 and CCSD(T) calculations. Upon selecting organic substrates to represent both volatile and nonvolatile iodocarbons, our calculations show that iodination by HOI is greatly favored as it gives strongly exoergonic reactions contrarily to what happens with I<sub>2</sub> or I<sub>3</sub><sup>−</sup>.

**Acknowledgment.** This research has been carried out with funding from the Spanish Ministry of Education, Project FIS2007-61686, Ministry of Science, Project BIO2009-07050, and Comunidad de Madrid, Grant EIADES S-0505/AMB/0296. O.G. acknowledges financial support from CSIC, "JAE-Doc" program.

**Supporting Information Available:** Ribbon diagram of VIPO protein. Modeled structure of VIPO protein in PDB format. AREP-optimized cc-pVTZ and aug-cc-pVTZ basis sets for iodine atom.  $\Delta_f H^0_0$ ,  $\Delta_f H^0_{298}$ ,  $H^0_{298}-H^0_0$ , and  $S^0_{298}$  values for species involved in reactions R1–R3. MP2 geometries and MP2 and CCSD(T) absolute energies calculated with aug-cc-pVTZ basis sets for species involved in reactions R1–R3. B3LYP/cc-pVTZ geometries and absolute energies of complexes **1–8** plus **1'** and **3'**. B3LYP/cc-pVTZ values of Gibbs free energies and energy corrections obtained in PCM calculations with  $\epsilon = 4, 40$ , and  $80$  for all the species involved in the catalytic cycle of VIPO (Schemes 2 and 3). This information is available free of charge via the Internet at <http://pubs.acs.org/>.

## References

- (1) (a) Chameides, W. L.; Davis, D. D. *J. Geophys. Res.* **1980**, *85*, 7383–7393. (b) Solomon, S.; Garcia, R. R.; Ravishankara, A. R. *J. Geophys. Res.* **1994**, *99* (D10), 20491–20500. (c) Vogt, R.; Sander, R.; von Glasow, R.; Crutzen, P. J. *J. Atmos. Chem.* **1999**, *32*, 375–395. (d) McFiggans, G.; Plane, J. M. C.; Allan, B. J.; Carpenter, L. J.; Coe, H.; O'Dowd, C. D. *J. Geophys. Res. Atmos.* **2000**, *105*, 14371–14385. (e) Calvert, J. G.; Lindberg, S. E. *Atmos. Environ.* **2004**, *38*, 5105–5116.
- (2) (a) Saiz-Lopez, A.; Plane, J. M. C. *Geophys. Res. Lett.* **2004**, *31*, L04112. (b) Saiz-Lopez, A.; Plane, J. M. C.; McFiggans, G.; Williams, P. I.; Ball, S. M.; Bitter, M.; Jones, R. L.; Hongwei, C.; Hoffmann, T. *Atmos. Chem. Phys. Discuss.* **2005**, *5*, 5405–5439. (c) Saiz-Lopez, A.; Plane, J. M. C.; McFiggans, G.; Williams, P. I.; Ball, S. M.; Bitter, M.; Jones, R. L.; Hongwei, C.; Hoffmann, T. *Atmos. Chem. Phys.* **2006**, *6*, 883–895.
- (3) Saiz-Lopez, A.; Boxe, C. S. *Atmos. Chem. Phys. Discuss.* **2008**, *8*, 2953–2976.
- (4) (a) Hoffmann, T.; O'Dowd, C. D.; Seinfeld, J. H. *Geophys. Res. Lett.* **2001**, *28*, 1949–1952. (b) O'Dowd, C. D.; Jimenez, J. L.; Bahreini, R.; Flagan, R. C.; Seinfeld, J. H.; Hameri, K.; Pirjola, L.; Kulmala, M.; Jennings, S. G.; Hoffmann, T. *Nature* **2002**, *417*, 632–636. (c) Jimenez, J. L.; Bahreini, R.; Cocker, D. R.; Zhuang, H.; Varutbangkul, V.; Flagan, R. C.; Seinfeld, J. H.; O'Dowd, C. D.; Hoffmann, T. *J. Geophys. Res.* **2003**, *108* (D10), 4318. (d) Burkholder, J. B.; Curtius, J.; Ravishankara, A. R.; Lovejoy, E. R. *Atmos. Chem. Phys.* **2004**, *4*, 19–34. (e) Saunders, R. W.; Plane, J. M. C. *Environ. Chem.* **2005**, *2*, 299–303.
- (5) (a) Saiz-Lopez, A.; Chance, K.; Liu, X.; Kurosui, T. P.; Sander, S. P. *Geophys. Res. Lett.* **2007**, *34*, L12812. (b) Saiz-Lopez, A.; Mahajan, A. S.; Salmon, R. A.; Bauguette, J. B.; Jones, A. E.; Roscoe, H. K.; Plane, J. M. C. *Science* **2007**, *317*, 348–351. (c) Schönhardt, A.; Richter, A.; Wittrock, F.; Kirk, H.; Oetjen, H.; Roscoe, H. K.; Burrows, J. P. *Atmos. Chem. Phys. Discuss.* **2007**, *7*, 12959–12999.
- (6) Whitehead, D. C. *Environ. Int.* **1984**, *10*, 321–339.
- (7) (a) Moore, R. M.; Groszko, W. J. *Geophys. Res.* **1999**, *104*, 11163–11171. (b) Aliche, B.; Hebestreit, K.; Platt, U. *Nature* **1999**, *397*, 572–573. (c) Allan, B. J.; Plane, J. M. C.; McFiggans, G. *Geophys. Res. Lett.* **2001**, *28*, 1945–1948. (d) Whalley, L. K.; Furneaux, K. L.; Gravestock, T.; Atkinson, H. M.; Bale, C. S. E.; Ingham, T.; Bloss, W. J.; Heard, D. E. *J. Atmos. Chem.* **2007**, *58*, 19–39. (e) Wada, R.; Beames, J. E.; Orr-Ewing, A. J. *J. Atmos. Chem.* **2007**, *58*, 69–87.
- (8) (a) McFiggans, G.; Coe, H.; Burgess, R.; Allan, B. J.; Cubison, M.; Alfarra, M. R.; Saunders, R.; Saiz-Lopez, A.; Plane, J. M. C.; Wevill, D. J.; Carpenter, L. J.; Rickard, A. R.; Monks, P. S. *Atmos. Chem. Phys.* **2004**, *4*, 701–713. (b) Carpenter, L. J.; Liss, P. S.; Penkett, S. A. *J. Geophys. Res.-Atmos.* **2003**, *108*, 4256.
- (9) Carpenter, L. J. *Chem. Rev.* **2003**, *103*, 4953–4962.
- (10) Leblanc, C.; Colin, C.; Cosse, A.; Delage La Barre, S.; Morin, P.; Fievet, B.; Voiseux, C.; Ambroise, Y.; Verhaeghe, E.; Amouroux, D.; Donard, O.; Tessier, E.; Potin, P. *Biochimie* **2006**, *88*, 1773–1785.
- (11) Küpper, F. C.; Carpenter, L. J.; McFiggans, G. B.; Palmer, C. J.; Waite, T. J.; Boneberg, E. M.; Woitsch, S.; Weiller, M.; Abela, R.; Grolimund, D.; Potin, P.; Butler, A.; Luther III, G. W.; Kroneck, P. M. H.; Meyer-Klaucke, W.; Feiters, M. C. *Proc. Natl. Acad. Sci. U.S.A.* **2008**, *105*, 6954–6958.
- (12) Küpper, F. C.; Schweigert, N.; Gall, E. A.; Legendre, J. M.; Vilter, H.; Kloareg, B. *Planta* **1998**, *207*, 163–171.
- (13) Palmer, C. J.; Anders, T. L.; Carpenter, L. J.; Küpper, F. C.; McFiggans, G. *Environ. Chem.* **2005**, *2*, 282–290.
- (14) Kylin, H. Z. *Physiol. Chem.* **1929**, *186*, 50–84.
- (15) Butler, A.; Carter-Franklin, N. *Nat. Prod. Rep.* **2004**, *21*, 180–188.
- (16) Colin, C.; Leblanc, C.; Michel, G.; Wagner, E.; Leize-Wagner, E.; Van Dorselaer, A.; Potin, P. *J. Biol. Inorg. Chem.* **2005**, *10*, 156–166.
- (17) Winter, J. M.; Moore, B. S. *J. Biol. Chem.* **2009**, *284*, 18577–18581.
- (18) Butler, A.; Sandy, M. *Nature* **2009**, *460*, 848–854.
- (19) Manley, S. L. *Biogeochem.* **2002**, *60*, 163–180.
- (20) (a) Faulkner, D. J. *Nat. Prod. Rep.* **2002**, *19*, 1–48. (b) Gribble, G. W. *Acc. Chem. Res.* **1998**, *31*, 141–152. (c) Carpenter, L. J.; Liss, P. S. *J. Geophys. Res.* **2002**, *105*, 20539–20547.
- (21) (a) Messerschmidt, A.; Wever, R. *Proc. Natl. Acad. Sci. U.S.A.* **1996**, *93*, 392–396. (b) Messerschmidt, A.; Prade, L.; Wever, R. *Biol. Chem.* **1997**, *378*, 309–315.
- (22) Macedo-Ribeiro, S.; Hemrika, W.; Renirie, R.; Wever, R.; Messerschmidt, A. *J. Biol. Inorg. Chem.* **1999**, *4*, 209–219.

- (23) Weyand, M.; Hecht, H.; Kiess, M.; Liaud, M.; Vilter, H.; Schomburg, D. *J. Mol. Biol.* **1999**, *293*, 595–611.
- (24) Isupov, M. N.; Dalby, A. R.; Brindley, A. A.; Izumi, Y.; Tanabe, T.; Murshudov, G. N.; Littlechild, J. A. *J. Mol. Biol.* **2000**, *299*, 1035–1049.
- (25) Carter, J. N.; Beatty, K. E.; Simpson, M. T.; Butler, A. *J. Inorg. Biochem.* **2002**, *91*, 59–69.
- (26) (a) Casny, M.; Rehder, D.; Schmidt, H.; Vilter, H.; Conte, V. *J. Inorg. Biochem.* **2000**, *80*, 157–160. (b) Rehder, D. *J. Inorg. Biochem.* **2008**, *102*, 1152–1158.
- (27) Kravitz, J. Y.; Pecoraro, V. L.; Carlson, H. A. *J. Chem. Theory Comput.* **2005**, *1*, 1265–1274.
- (28) Zampella, G.; Kravitz, J. Y.; Webster, C. E.; Fantucci, P.; Hall, M. B.; Carlson, H. A.; Pecoraro, V. L.; De Gioia, L. *Inorg. Chem.* **2004**, *43*, 4127–4136.
- (29) Zampella, G.; Fantucci, P.; Pecoraro, V. L.; De Gioia, L. *J. Am. Chem. Soc.* **2005**, *127*, 953–960.
- (30) Zampella, G.; Fantucci, P.; Pecoraro, V. L.; De Gioia, L. *Inorg. Chem.* **2006**, *45*, 7133–7143.
- (31) Zhang, Y.; Gascon, J. A. *J. Inorg. Biochem.* **2008**, *102*, 1684–1690.
- (32) Butler, A. *Coord. Chem. Rev.* **1999**, *187*, 17–35.
- (33) Hasan, Z.; Renirie, R.; Kerkman, R.; Ruijsenaars, H. J.; Hartog, A. F.; Wever, R. *J. Biol. Chem.* **2006**, *281*, 9738–9744.
- (34) Itoh, N.; Hasan, A. K.; Izumi, Y.; Yamada, H. *Eur. J. Biochem.* **1988**, *172*, 477–484.
- (35) De Boer, E.; Wever, R. *J. Biol. Chem.* **1988**, *263*, 12326–12332.
- (36) Peroxibase - The Peroxidase database. <http://peroxibase.toulouse.inra.fr/index.php> (accessed Jun. 9, 2009).
- (37) (a) Swiss-Model. <http://swissmodel.expasy.org> (accessed Jun. 9, 2009). (b) Arnold, K.; Bordoli, L.; Kopp, J.; Schwede, T. *Bioinform.* **2006**, *22*, 195–201. (c) Kiefer, F.; Arnold, K.; Kunzli, M.; Bordoli, L.; Schwede, T. *Nucl. Acid. Res.* **2009**, *37*, D387–D392.
- (38) Pettersen, E. F.; Goddard, T. D.; Huang, C. C.; Couch, G. S.; Greenblatt, D. M.; Meng, E. C.; Ferrin, T. E. *J. Comput. Chem.* **2004**, *25*, 1605–1612, Chimera, version 1.3; UCSF Chimera. <http://www.cgl.ucsf.edu/chimera/> (accessed Sep. 9, 2009).
- (39) DeLano, W. L. *PyMOL*, version 1.2r1; DeLano Scientific LLC: Palo Alto, CA, 2009. PyMOL Molecular Viewer. <http://www.pymol.org> (accessed Oct. 26, 2009).
- (40) Pacios, L. F. *Comput. Chem.* **1994**, *18*, 377–385.
- (41) Tsodikov, O. V.; Record, M. T.; Sergeev, Y. V. *J. Comput. Chem.* **2002**, *23*, 600–609.
- (42) Baker, N. A.; Sept, D.; Holst, J. S.; McCammon, J. A. *Proc. Natl. Acad. Sci. U.S.A.* **2001**, *98*, 10037–10041.
- (43) Wang, J.; Cieplak, P.; Kollman, P. A. *J. Comput. Chem.* **2000**, *21*, 1049–1074.
- (44) Dolinsky, T. J.; Nielsen, J. E.; McCammon, J. A.; Baker, N. A. *Nucl. Acid. Res.* **2004**, *32*, W665–W667.
- (45) (a) Davis, M. E.; McCammon, J. A. *Chem. Rev.* **1990**, *94*, 7684–7692. (b) Honig, B.; Nicholls, A. *Science* **1995**, *268*, 1144–1149.
- (46) Breneman, C. M.; Wiberg, K. B. *J. Comput. Chem.* **1990**, *11*, 361–36.
- (47) Balabanov, N. B.; Peterson, K. A. *J. Chem. Phys.* **2005**, *123*, 064107/1–15.
- (48) Pacios, L. F.; Christiansen, P. A. *J. Chem. Phys.* **1985**, *82*, 2664–2671.
- (49) LaJohn, L. A.; Christiansen, P. A.; Ross, R. B.; Atashroo, T.; Ermler, W. C. *J. Chem. Phys.* **1987**, *87*, 2812–2824.
- (50) (a) Ermler, W. C.; Ross, R. B.; Christiansen, P. A. *Adv. Quantum Chem.* **1988**, *19*, 139–182. (b) Christiansen, P. A. *J. Chem. Phys.* **2000**, *112*, 10070–10074.
- (51) Martin, J. M. L.; Sundermann, A. *J. Chem. Phys.* **2001**, *114*, 3408–3420.
- (52) Werner, H. J.; Knowles, P. J.; Lindh, R.; Manby, F. R.; Schütz, M.; Celani, P.; Korona, T.; Rauhut, G.; Amos, R. D.; Bernhardsson, A.; Berning, A.; Cooper, D. L.; Deegan, M. J. O.; Dobbyn, A. J.; Eckert, F.; Hampel, C.; Hetzer, G.; Lloyd, A. W.; McNicholas, S. J.; Meyer, W.; Mura, M. E.; Nicklass, A.; Palmieri, P.; Pitzer, R.; Schumann, U.; Stoll, H.; Stone, A. J.; Tarroni, R.; Thorsteinsson, T. *MOLPRO*, version 2006.1; MOLPRO quantum chemistry package. <http://www.molpro.net> (accessed Sep. 15, 2008).
- (53) Curtiss, L. A.; Raghavachari, K.; Redfern, P. C.; Pople, J. A. *J. Chem. Phys.* **1997**, *106*, 1063–1079.
- (54) Chase, M. W., Jr. *J. Phys. Chem. Ref. Data* **1998**, *9*, 1–1951.
- (55) Frisch, M. J.; Trucks, G. W.; Schlegel, H. B.; Scuseria, G. E.; Robb, M. A.; Cheeseman, J. R.; Montgomery, J. A., Jr.; Vreven, T.; Kudin, K. N.; Burant, J. C.; Millam, J. M.; Iyengar, S. S.; Tomasi, J.; Barone, V.; Mennucci, B.; Cossi, M.; Scalmani, G.; Rega, N.; Petersson, G. A.; Nakatsuji, H.; Hada, M.; Ehara, M.; Toyota, K.; Fukuda, R.; Hasegawa, J.; Ishida, M.; Nakajima, T.; Honda, Y.; Kitao, O.; Nakai, H.; Klene, M.; Li, X.; Knox, J. E.; Hratchian, H. P.; Cross, J. B.; Bakken, V.; Adamo, C.; Jaramillo, J.; Gomperts, R.; Stratmann, R. E.; Yazyev, O.; Austin, A. J.; Cammi, R.; Pomelli, C.; Ochterski, J. W.; Ayala, P. Y.; Morokuma, K.; Voth, G. A.; Salvador, P.; Dannenberg, J. J.; Zakrzewski, V. G.; Dapprich, S.; Daniels, A. D.; Strain, M. C.; Farkas, O.; Malick, D. K.; Rabuck, A. D.; Raghavachari, K.; Foresman, J. B.; Ortiz, J. V.; Cui, Q.; Baboul, A. G.; Clifford, S.; Cioslowski, J.; Stefanov, B. B.; Liu, G.; Liashenko, A.; Piskorz, P.; Komaromi, I.; Martin, R. L.; Fox, D. J.; Keith, T.; Al-Laham, M. A.; Peng, C. Y.; Nanayakkara, A.; Challacombe, M.; Gill, P. M. W.; Johnson, B.; Chen, W.; Wong, M. W.; Gonzalez, C.; Pople, J. A. *GAUSSIAN03*; Gaussian Inc.: Wallingford, CT, 2004.
- (56) Bordoli, L.; Kiefer, F.; Arnold, K.; Benkert, P.; Batterly, J.; Schwede, T. *Nature Protocols* **2009**, *4*, 1–14.
- (57) Hasan, Z.; Renirie, R.; Kerkman, R.; Ruijsenaars, H. J.; Hartog, A. F.; Wever, R. *J. Biol. Chem.* **2006**, *281*, 9738–9744.
- (58) Waller, M. P.; Bühl, M.; Geethalakshmi, K. R.; Wang, D.; Thiel, W. *Chem.—Eur. J.* **2007**, *13*, 4723–4732.
- (59) Waller, M. P.; Geethalakshmi, K. R.; Bühl, M. J. *J. Phys. Chem. B* **2008**, *112*, 5813–5823.
- (60) Colpas, G. J.; Hamstra, B. J.; Kampf, J. W.; Pecoraro, V. L. *J. Am. Chem. Soc.* **1996**, *118*, 3469–3478.
- (61) Hemrika, W.; Renirie, R.; Macedo-Ribeiro, S.; Messerschmidt, A.; Wever, R. *J. Biol. Chem.* **1999**, *274*, 23820–23827.
- (62) Martinez, J. S.; Carrol, G. L.; Tschirret-Guth, R. A.; Altenhoff, G.; Little, R. D.; Butler, A. *J. Am. Chem. Soc.* **2001**, *123*, 3289–3294.



- (63) Everett, R. R.; Soedjak, H. S.; Butler, A. *J. Biol. Chem.* **1990**, *265*, 15671–15679.
- (64) Tschirret-Guth, R. A.; Butler, A. *J. Am. Chem. Soc.* **1994**, *116*, 411–412.
- (65) Martinez, V. M.; De Cremer, G.; Roeffaers, M. B.; Sliwa, M.; Baruah, M.; De Vos, D. E.; Hofkens, J.; Sels, B. F. *J. Am. Chem. Soc.* **2008**, *130*, 13192–13193.
- (66) Huber, K. P.; Herzberg, G. *Constants of Diatomic Molecules*; Van Nostrand Reinhold: New York, 1979; pp 330–333.
- (67) Asaduzzaman, A. M.; Schreckenbach, G. *Theor. Chem. Acc.* **2009**, *122*, 119–125.
- (68) Do, K.; Klein, T. P.; Pommerening, C. A.; Sunderlin, L. S. *J. Am. Soc. Mass Spectrom.* **1997**, *8*, 688–696.
- (69) Lynden-Bell, R. M.; Kosloff, R.; Ruhman, S.; Danovich, D.; Vala, J. *J. Chem. Phys.* **1998**, *109*, 9928–9937.
- (70) Toyota, K.; Kanaya, Y.; Takahashi, M.; Akimoto, H. *Atmos. Chem. Phys.* **2004**, *4*, 1961–1987.
- (71) Gilfedder, B. S.; Lai, S. C.; Petri, M.; Biester, H.; Hoffmann, T. *Atmos. Chem. Phys.* **2008**, *8*, 6069–6084.

CT100041X